On the mechanism behind the shift of the turbidity maximum zone in response to reclamations in the Yangtze (Changjiang) Estuary, China

Teng Lizhi[a], Cheng Heqin[a, b,*], Huib E. de Swart[c], Ping Dong[d], Li Zhanhai[a], Li Jiufa[a], Wang Yajun[a]

[a] State Key Laboratory of Estuarine and Coastal Research, East China Normal University, Shanghai 200241, China.

[b] Institute of Eco-Chongming, East China Normal University, Shanghai 202162, China.

[c] Institute for Marine and Atmospheric Research, Utrecht University, Princetonplein 5, 3584 CC, Utrecht, the Netherlands.

[d] School of Engineering, University of Liverpool, Liverpool, L69 3GH, UK.

[*]Corresponding author: Cheng Heqin

Tel: +86 21 54836006

Fax: +86 21 54836006

E-mail address: hqch@sklec.ecnu.edu.cn

Highlights

1. The landward boundary of turbidity maximum zone has moved seawards.

2. Ebb dominance is enhanced in the deep channel via channel narrowing and deepening.

3. Coarsening of surface sediments has weakened resuspension.

Abstract

Reclamation in estuaries can greatly change the channel geometry and hydrodynamic conditions and these changes may have significant impacts on spatial and temporal distribution of the turbidity maximum zone. This study focuses on the effects of a large area of reclamation built in 2007-2018 and the behavior of the turbidity maximum zone along the North Channel of the Yangtze Estuary. Data were collected bathymetry in the North Channel, tidal elevations at Sheshan Station, river discharge at Datong Station and turbidity, retrieved from six Landsat remote sensing images in the dry season from 2006 to 2019. In-situ measured data on flow velocity and suspended sediment concentration were obtained in the dry season of 2003, 2012 and 2018. Analysis of the data revealed that reclamations, which led to narrowing (0.86-2.74 km) and fixing of the channel, caused erosion of 0.19-3.72 m in the deep channel and deposition on the tidal flats. Furthermore, it was found that the length of the turbidity maximum zone decreased: its landward boundary shifted 5 km seaward during spring tide and 17 km seaward during neap tide in the dry season, and the position of the seaward boundary wandered within a range of 3 km, being further downstream during the neap tide than that during the spring tide. A conceptual model of changes in the borders of the turbidity maximum zone in response to reclamation is proposed. After construction of the reclamation, the deeper and narrower channel intensified ebb-dominance of the flow velocity. The coarsening of bed sediment weakened resuspension and decreased the bottom tidally averaged suspended sediment concentration. These changes led to a significant decline in the depth-mean of tidally averaged suspended sediment concentration and caused the seaward movement of the landward boundary of the turbidity maximum zone.

Keywords

Suspended sediment; Estuarine engineering; Channel geometry; Remote sensing images

1. Introduction

The turbidity maximum zone (TMZ) is the region within an estuary where the suspended sediment concentration (SSC) is significantly higher than that in adjacent waters. The TMZ is formed as a result of sediment accumulating under the dynamic interaction between runoff, stratification and tide and it regularly migrates within a certain range (Li and Zhang, 1998; Doxaran et al., 2009). The dynamics of suspended sediment in the TMZ plays an important role in the morphological evolution of the channel and shoals (Wu et al., 2012), as well as in the transport of nutrients and pollutants (Gebhardt et al., 2005). The TMZ has been observed and studied in many estuaries around the world (Burchard et al. 2018 and references herein) and measurements of its spatial distribution are often used as a reference for maintaining navigation channels (de Jonge et al., 2014) and for ecological conservation (Mitchell, 2013).

It is well established that land reclamation projects conducted in estuaries modify the channel geometry and alter the hydrodynamics and accumulation of sediment (Williams et al., 2015; Gao et al., 2018). For example, the tidal-choking effect of reclamation caused a decrease in flood dominance within the main branch of the Yalu River Estuary (Cheng et al., 2020) and reclamation in the Ems estuary decreased the area of subtidal flats by reducing the amount of fine-grained sediment deposited (van Maren, et al., 2016). However, the effect of reclamation on changes in the characteristics of the TMZ, such as shifts of its borders and location and intensity of the maximum SSC, has hardly been studied. A series of reclamation projects has been conducted in the Yangtze

Estuary (YE) since the 1990s. During this period, the land area in the YE has increased by 10% (Zhang et al., 2020), the growth rate of the subtidal zone has decreased from 6.0 km^2 yr^{-1} (1977–1994) to -6.2 km^2 yr^{-1} (1994–2011) (Du et al., 2016), and the slope of tidal flats between the -2 m and -3 m isobaths has become steeper (Wei et al., 2017). Most notably the channel geometry of the North Channel (NC) of the YE has been strongly modified over the past two decades by reclamation projects, such as the Qingcaosha Reservoir and the Hengsha East Shoal Promoting Siltation project (HESP) (Wu et al., 2016). Only minor artificial dredging takes place in the NC so variations in geometry of the NC prior to reclamation works can be regarded as being natural (Mei et al., 2018). This makes the NC a suitable area to study the spatial change mechanism of the TMZ in response to estuarine reclamation. The specific aims of this study are to quantify and explain, in the case of the NC, how reclamation changed 1) erosion-deposition patterns, 2) the length of the TMZ, both during spring and neap tide, 3) the flow, in particular its ebb/flood dominance, 4) the tidally averaged suspended sediment concentrations and 5) the composition of the bed sediment. The focus was on the dry season, as in the Yangtze River basin there have been minimal changes in the river discharge during that season since the Three Gorges Project and construction of fresh water reservoirs were completed (Guo et al., 2018).

Changes in channel morphology due to reclamations were derived from bathymetric data. Clearly, in-situ observations are most useful to assess variations in hydrodynamics and sediment dynamics between pre- and post-engineering. However, due to the lack of spatial coverage they cannot provide a macro view of the surface suspended sediment concentration (SSSC) distribution. Therefore, this study also uses remote sensing data of suitable spatial coverage at various time intervals (Wackerman et al., 2017). In the analyses conducted in this study, both Landsat remote sensing images and in situ measured data from the dry season were used. Combined with the spatial changes of TMZ and the variations of hydrodynamics and sediment dynamics between pre- and post-reclamations, the mechanism behind the shift of the TMZ in response to reclamation was unraveled.

The remainder of this paper is organized as follows. Section 2 introduces the geographical setting of the NC, including the information about the large-scale estuarine reclamation projects conducted in the NC over the past two decades. The methods used are presented in Section 3. Next, Section 4 describes the variations in channel geometry and spatial distribution of the TMZ of the NC post-reclamation. It further presents the changes in the hydrodynamic and vertical profiles of the tidally averaged suspended sediment concentration in the NC, as well as a grain size analysis of bed sediments. Section 5 discusses the spatial changes mechanism of the TMZ in response to reclamation in estuaries and proposes a conceptual model. Finally, Section 6 presents the conclusions.

2. Geographical Setting

The Yangtze River has a length of approximately 6300 km. The YE is a mesotidal estuary (Luan et al., 2016) with a length of 90 km, a width of 90 km at its outer limit (Figure 1b). Tidal range in the YE is in the range 2-3.83 m (Cheng et al., 2018). The annual average runoff between 2009 and 2019 was 8.89×10^{11} m^3 and observational data from Datong gauging station show that the annual average sediment transport decreased from 4.22×10^8 t yr^{-1} (2003–2019) to 1.32×10^8 t yr^{-1} (2003–2019) (Zheng et al., 2018). The YE has developed a three-order bifurcation and four-outlet configuration downstream. First, the YE is divided into North Branch (NB) and South Branch

(SB) by Chong Ming Island. The South Branch is further divided into the North Channel (NC) and South Channel (SC) by Changxing and Hengsha Island. The South Channel is followed by the North Passage (NP) and South Passage (SP), which are separated by the Jiuduansha shoal (Figure 1b). The NC is part of the second-order bifurcation with a length of 70 km (Wang et al., 2013). Approximately fifty percent of the runoff from the Yangtze River flows through the NC in the YE into the East China Sea (Wu et al., 2016).

The dates and locations of major engineering projects are shown in Table 1, from which it is evident that most of these projects began in 2005 and 2007. According to the magnitude of the tidal flow and the location of the project, the NC is divided into three segments (Figure 1c). The upper segment is located near the Qingcaosha Reservoir, where runoff is strong. The middle segment is situated downstream of the Qingcaosha Reservoir. Finally, the lower segment is located near the Hengsha Shoal (HESP), where the effect of tidal flow is largest.

3. Materials and methods

3.1. Bathymetric data and variations in channel morphology

Bathymetric data of the NC between Baozhen and the outer estuary of the NC (Figure 1c) were obtained from navigation maps compiled by the China Maritime Safety Administration (China MSA) in 1995, 2007 and 2018. These navigation maps have a scale of 1:25000 and the base levels provided are the theoretical depth datum, which is the lowest water level obtained from a combination of 13 gauging stations within the YE.

After geometric correction of navigation maps, shoreline and bathymetry data were transformed into a Universal Transverse Mercator Grid System (UTM) via the WGS84 coordinate system in ArcGIS. Digital elevation models (DEM) with a resolution of 200 m × 200 m were established through Kriging interpolation (e.g. Webster and Oliver, 2007). Deposition and erosion patterns during the period were then obtained by subtracting the previous morphological surveys. Positive values indicate depth reduced resulted from deposition, vice versa. The large-scale reclamation projects, such as the Qingcaosha Reservoir and the HESP, both began in 2007. So the impact of reclamations on channel morphology could be analyzed based on the variations of deposition and erosion patterns between pre- and post-reclamations.

3.2. Processing of remote sensing images and defining the TMZ

3.2.1. Selection of remote sensing images and estimating SSSC

The SSSC distributions in the years 2006 to 2019 within the YE were derived from remote sensing images obtained by Enhanced Thematic Mapper (ETM) of Landsat 7 with a spatial resolution of 30 m (Table 2).

The SSSC in the YE strongly differs between wet and dry seasons, spring and neap tides and between ebb and flood tides (Shen et al., 2013). To compare and analyze annual variations in the spatial distribution of the TMZ, we selected six remote sensing images that were similar in terms of the river discharge, the tide type and the time at which the images were taken.

Regarding river discharge, data were used of Datong gauging station, which is located 600 km upstream of the YE (Figure 1a) and is generally considered to be the landward boundary of tidal impact. It is the runoff and sediment inflow control station of the YE. This study used river discharge recorded at Datong Station on the same dates as that the remote sensing images were taken. Data about the tides (sea surface variations) on these dates were taken of Sheshan gauging station. The latter is located outside the YE (Figure 1a), where the tidal characteristics are less affected by reclamation projects (Cheng et al., 2018).

After precise geometric correction of the remote sensing images, the gray value, DN, of the original images was converted to radiance through radiometric calibration as

$$L = \text{gains} \times \text{DN} + \text{bias}.$$

In this expression, L is the pixel radiance value of remote sensing images and DN is the pixel gray. The value of the gains and bias were obtained from the header file of the remote sensing image. The FLASH module in ENVI software was used to correct the pixel radiance for influence from the atmosphere, which resulted in surface reflectance. The SSSC in the YE has obvious peaks in reflectance to band 4 (760–900 nm) and band 3 (630–690 nm) of Landsat ETM and the fitting degree of regression between the SSSC and the ratio of surface reflectance in these two bands (TM4/TM3) is high (Shen et al., 2013). Therefore, a linear regression equation was used to estimate the SSSC based on the surface reflectance of ETM bands 3 and 4,

$$SSSC = 2.2979x^2 - 2.2950x + 0.6206,$$

where x is the ratio of surface reflectance of Landsat ETM bands 4 and 3 (TM4/TM3). The correlation between SSSC and the measured data is 0.92 and thus, use of this equation is effective in the YE (Shen et al., 2013).

3.2.2. Definition of the TMZ

The area that has a significantly higher SSSC compared with the adjacent water in the inversion results of remote sensing images is called the TMZ (Doxaran et al., 2009). To make this more quantitative, it is important to realize that there are long-term trends in SSSC. Due to the retaining effect of large-scale projects in the basin, and particularly that of the Three Gorges Dam after 2003, there has been a continuous decrease in the sediment transport into the YE. This led to an overall reduction of the SSSC (Yang et al., 2010) and the area where SSSC is larger than 0.7 kg m^{-3} reduced by 23% (Jiang et al., 2013). To avoid the influence of the overall reduction in SSSC on determining the TMZ, the SSSC values derived from remote sensing images were converted into relative SSSC values (RSSSC) as

$$RSSSC = SSSC/ASSSC.$$

Here, *ASSSC* is the area-averaged SSSC within the NC. TMZ is defined as the area where *SSSC* is larger than *ASSSC*, so where $RSSSC > 1$ As the TMZ of the YE is strongly affected by spring and neap tides (Jiang et al., 2013), the inversion results of remote sensing images in different years were divided into two groups (taken during spring and neap tide, respectively) to calculate the annual variation in the spatial distribution of the TMZ that occurred after completion of the reclamation projects.

3.3. Collection of hydrodynamic data and sediment concentration data

3.3.1. In-situ observations of flow velocity and suspended sediment concentration (SSC)

Vertical profiles of flow velocity and SSC during 25 h were continuously and synchronously observed in 2003 and 2018 (Figure 1c and Table 3). Station BG1was in upper segment and station

BG2 was in the middle segment, station BG3 and BG4 were in the lower segment. They were used to assess the impact of reclamations on hydrodynamics and sediment dynamics. However, there was a lack of flow velocity profiles at station BG2 in 2003. The daily averaged tidal range was calculated as the average of four observed tidal ranges (two tidal cycles). Daily averaged wave heights during the times of observations were calculated from the dataset of European Centre for Medium-Range Weather Forecasts (ECMWF). During the different observation periods, wave conditions and river discharges were similar during spring tide and neap tide, respectively (Table 3). In tidal estuaries, the wind force potentially has a strong influence on estuarine circulation (Lange and Burchard, 2019; Zhang et al., 2019). Because wind speeds during observations were generally weak, the wind influence on circulation was not considered in this paper. The in-situ velocity data were obtained using an Acoustic Doppler Current Profiler (ADCP) fixed on one side of a boat using a steel fixing frame. Vertical profiles of turbidity were obtained every hour with an Optical Backscatter Sensor (OBS). The SSC at different depths was estimated according to the regression relation between the SSC and the turbidity obtained by the OBS calibrated in the laboratory.

The characteristics of surface sediment were obtained from samples (2 mm layer) along the main channel of the NC using a box dredger in April 2018 (Figure 1c). The particle size distribution of the sediment was determined by using a laser particle size analyzer (LS13320) in the laboratory. The surface sediment was classified according to Folk et al. (1970).

3.3.2. The coefficient of flow dominance

Under the action of the longitudinal surface slope, the longitudinal density gradient and tidal mixing, there is significant estuarine circulation in the lower segment during the dry season. The residual current in the upper layer points seaward, whereas the lower layer residual current is directed landward. A large amount of sediment occurs in the area where landward and bottom flow meet, thereby forming the TMZ (Jiang et al., 2013; Li et al., 2019). The coefficient of flow dominance, R reflects the degree of the ebb dominance in a tidal cycle under the same river discharge (Mei et al., 2018). The dominant flow coefficient R was calculated as

$$R = E/(E + F),$$

where E is the distance travelled by a particle during an ebb period and F the distance travelled by a water particle during flood tide:

$$E = \int_0^{T_E} V_E \cos\theta \, dt,$$

$$F = \int_0^{T_F} V_F \cos\theta \, dt.$$

Here, T_E and T_F are the ebb and flood period, V_E and V_F are the ebb and flood flow velocity and θ is the angle between the flow direction and the long axis direction of the tide. The flow is ebb-dominant when $R > 0.5$, otherwise it is flood-dominant. Note that V_E, V_F and θ are considered at different points on a vertical section.

The along-channel location where the coefficient of flow dominance near the bottom is 0.5 can be interpreted as the stagnation point of the near-bottom flow. In a previous study by Shen et al. (1992) it was already demonstrated that this stagnation point is close to the core of the TMZ. As the daily average discharges observed at Datong gauging station during the observations were similar in 2003 and 2012 (Table 3), the variations in the strengths of the ebb and flood flow could be analyzed by comparing the dominant flow coefficients in different years.

4. Results

4.1. Variations of erosion-deposition patterns associated with reclamations

Before the execution of a series of reclamation projects, between 1995 and 2007, there was area-integrated erosion observed in the upper and middle segments and area-integrated deposition in the lower segment (Figure 2a). The strongest amount of erosion (volume change of -1.5×10^{7} m^3) occurred in 27-28 km downstream of the starting point of NC. The largest amount deposited (volume change of 3.6×10^{6} m^3) occurred in 36-37 km downstream of the starting point (Figure 2g).

In the upper segment, deposition mainly occurred on the shoal near the south bank, while erosion occurred in the channel along the north bank (Figure 2a). The rates of volume change below the depth of 0 m and -5 m were -1.08×10^{7} m^3 yr^{-1} and -1.07×10^{7} m^3 yr^{-1}(Figures 2d-2e). In the middle and lower segments, there was deposition on the shoal near the north bank, while erosion occurred in the channel along the south bank (Figure 2a). In the middle segment, the rates of volume change below the depth of 0 m and -5 m were -5.75×10^{6} m^3 yr^{-1} and -4.30×10^{6} m^3 yr^{-1} (Figures 2d-2e), respectively. In the lower segment, the rates of volume change below the depth of 0 m and -5 m were -1.29×10^{5} m^3 yr^{-1} and -1.07×10^{6} m^3 yr^{-1} (Figures 2d-2e).

After the construction of the Qingcaosha Reservoir and HESP, from 2007 to 2018, the strongest erosion (volume change of 1.22×10^{7} m^3) occurred in 41-42 km downstream of the starting point and deposition was the strongest (volume change of -4.43×10^{6} m^3) in 37-38 km from the starting point (Figure 2h).

Due to the construction of Qingcaosha Reservoir and the growth of its outer shoal (Figure 2b), the rate of volume change below 0 m was 3.21×10^{6} m^3 yr^{-1} in the upper segment (Figure 2d). The volume change rate below a depth of -5 m was -3.97×10^{6} m^3 yr^{-1} (Figure 2e). The rate of volume changes below depth of 0 m and -5 m were -0.95×10^{7} m^3 yr^{-1} and -1.13×10^{7} m^3 yr^{-1} in the middle segment (Figures 2d-2e). The erosion rate of the channel below a depth of -5 m increased more than 150 % after reclamations. Meanwhile, the lower segment transformed from a region-integrated deposition to a region-integrated erosion (Figures 2g-2h). The erosion rate of the channel below a depth of -5 m increased more than 600 % after reclamations. These findings provide support for the hypothesis that constructions of reclamations intensified the erosion in the channel. However, the volume below the depth of 0 m was 6.20×10^{5} m^3 yr^{-1} (Figure 2d) due to deposition of the tidal flat near the north bank (Figure 2b). The volume change rate below the -5 m isobaths was -7.86×10^{6} m^3 yr^{-1} (Figure 2e). Furthermore, the volume change rate below the -10 m isobaths was -1.48×10^{5} m^3 yr^{-1} (Figure 2f).

4.2. Changes in the locations of boundaries of the TMZ

4.2.1. TMZ during spring tide

In 2006, the *ASSSC* of NC was 0.32 kg m^{-3} during spring tide in the dry season (Figure 3a). The landward boundary of the TMZ was located at 121°52′ E (36 km to the begin point), the seaward boundary was at 122 °12 ′ E (66 km to the begin point), the length of the TMZ was reduced to 30 km (Figures 3d and 3g). After the completion of Qingcaosha Reservoir and the sixth phase of the HESP, the *ASSSC* reduced to 0.18 kg·m^{-3} in 2011 (Figure 3b). The landward boundary of the TMZ moved seawards by 9 km to 121°59 E, the landward boundary of the TMZ moved seawards by 5 km to 122°14′ E and the length of the TMZ was 26 km (Figures 3e and 3h). By 2019, the *ASSSC* decreased to 0.11 kg m^{-3} (Figure 3c). The length of the TMZ was 24 km, with the landward boundary located at 121 ° 58 E and the seaward boundary located at 122 ° 12 E (Figures 3f and 3i). The landward boundary moved landwards by 3 km, and the seaward boundary moved landwards by 5 km.

From 2006 to 2019, during spring tide, the landward boundary of the TMZ moved seaward by 6 km and the location of the seaward boundary presently wanders within a 3 km range from 122° 12' E to 122° 14' E.

4.2.2. TMZ during neap tide

In 2006, the *ASSSC* of NC was 0.15 kg m^{-3} (Figure 4a), the landward boundary of the TMZ was 121°59 E (47 km to the begin point), the seaward boundary was 122°24′ E (84 km to the begin point) and the length of the TMZ was 37 km (Figures 4d and 4g). In 2011, the *ASSSC* had decreased to 0.08 kg m^{-3} (Figure 4b), the landward boundary of the TMZ had moved 5 km seawards to 122°3′ E, the seaward boundary of the TMZ had moved 2 km landwards to 122°23′ E and the extent of TMZ had shrunk to 33 km (Figures 4e and 4h). By 2017, the *ASSSC* had decreased to 0.10 kg m^{-3} (Figure 4c). The landward boundary had moved 12 km seawards to 122°9 E (Figure 4f), but there was no change in the seaward boundary (Figure 4i).

From 2006 to 2017, during neap tide, the landward boundary of the TMZ moved seaward by 17 km and the seaward boundary of the TMZ wandered in the range of 122° 23' E to 122° 24' E. The SSSC within the TMZ during neap tide was always lower than that during spring tide and the TMZ during neap tide was located downstream of that during spring tide.

4.3. Changes in the dominant flow

Before the execution of a series of reclamation projects, in 2003, the values of the dominant flow coefficient R during spring tide at station BG1 were between 0.49 and 0.52 (Figure 5a), so the stagnation point of near-bottom flow was closely located to this station. The values of R at station BG1 were 0.61 to 0.64 during the neap tide, which showed that the ebb flow was dominant (Figure 5a). In the lower segment, the values of R at station BG3 were between 0.49 and 0.52 during spring tide (Figure 5b). During neap tide, the values of R below -0.5 depth were between 0.34 and 0.45, which shows that the flow was flood dominant (Figure 5b). In addition, there was an obvious estuarine circulation at BG3 station.

After the construction of the Qingcaosha Reservoir and the EHSP, in 2018, values of the dominant flow coefficient R at station BG1 were between 0.68 to 0.71 during spring tide and between 0.76 to 0.78 during neap tide (Figure 5c). Thus, with respect to earlier years, the ebb dominance increased. Values of R at station BG2 ranged from 0.63 to 0.65 during spring tide and 0.69 to 0.72 during neap tide (Figure 5d). Although station BG4 was 9 km downstream of BG3, the values of R at this station were between 0.62 and 0.65 in spring tide and between 0.51 and 0.63 during neap tide (Figure 5e). Conditions were ebb-dominant at three stations during spring tide and neap tide; the stagnation point moved to a location downstream of the station BG4.

4.4. Changes in the tidally averaged SSC

According to the in-situ observations in 2003 and 2018 (Figure 7), after the construction of

Qingcaosha Reservoir and completion of the HESP, there was a decline of tidally averaged SSC within the NC. At station BG1, located in the upper segment, the depth-mean of tidally averaged SSC decreased from 0.34 kg m^{-3} to 0.22 kg m^{-3} during spring tide conditions and decreased from 0.12 kg m^{-3} to 0.18 kg m^{-3} during neap tide conditions (Figures 7a and 7d). At station BG2, located in the middle segment, the depth-mean of tidally averaged SSC decreased from 0.63 kg m^{-3} to 0.32 kg m^{-3} over spring tide and decreased from 0.26 kg m^{-3} to 0.19 kg m^{-3} over neap tide (Figures 7b and 7e). In the lower segment, in 2003, the depth-mean of the tidally averaged SSC at BG3 was 1.00 kg m^{-3} during spring tide and 0.37 kg m^{-3} during neap tide (Figure 7c). In 2018, the depth-mean of tidally averaged SSC of station BG4 was 0.82 kg m^{-3} during spring tide and 0.48 kg m^{-3} during neap tide (Figure 7f).

In 2003, the tidally averaged SSC at station BG2 during spring tide was 0.32 kg m^{-3} in the surface layer and 1.07 kg m^{-3} in the bottom layer (Figure 7b). The vertical profile of tidally averaged SSC during neap tide showed a two-layer structure, with values of 0.16 kg m^{-3} near the surface and 0.96 kg m^{-3} near the bottom layer (Figure 7b). After the construction of a series of reclamation projects, the tidally averaged SSC near the bottom significantly decreased by 0.59 kg m^{-3} during spring tide and 0.77 kg m^{-3} during the neap tide (Figure 7e). Therefore, in station BG2, where the landward boundary of the TMZ prior to the reclamations was located, the depth-mean tidally averaged SSC decreased significantly over spring and neap tide.

4.5. Changes in characteristics of bed sediment

Measured data obtained in the dry season of 2003 showed that the median grain size of bed sediments was 126.2 μm and 16.5 μm in the middle and lower segments, respectively (Liu et al., 2010). The measured data obtained in the dry season of 2018 showed that the bed sediment in middle segment was silty sand with a median grain size of 178.8 μm, but the sediment in lower segment was finer (sandy silt and silt with a median grain size of 18.2 μm). Coarser particles accounted for a large proportion of the sediment in all samples, as the skewness was negative. Thus, in the period 2003-2018, the bed sediment coarsened significantly in the middle segment. However, the change of the mean grain size of the surface sediment in the lower segment was small.

5. Discussion

5.1. Comparison with other estuaries

Land reclamations generally change the distribution of SSC, because they modify the morphology of an estuary. In e.g. the Ems estuary, located at the border between Germany and the Netherlands, it was found that the SSC increased due to the decrease in accommodation space for fine-grained sediments by land reclamations (Van Maren et al., 2016). Constructions of land reclamations in Ribble estuary (Van der Wal et al., 2002), Dee Estuary and Wash Estuary (Pye and Blott, 2014), all in the United Kingdom, reduced the tidal prism, leading to a reduction in average current speeds and accelerated sedimentation outside the embankments.

5.2. Changes in flow dominance and location of the stagnation point

The construction associated with the EHSP has fixed the southern boundary of the channel in the middle and lower segments. Therefore, the natural trend of the southward movement of the channel was limited. The reclamation intercepted flow and sediment exchange between the shoal and channel, which resulted in continuous erosion and an increase in the average water depth in the channel (Wu et al., 2016; Wei et al., 2017; Zhao et al., 2018). At the same time, deposition occurred near the northern band of the middle and lower segments. This happened because these areas were less affected by changes in the morphology and hydrodynamics of the channel and there was supply of offshore sediment (Zhu et al., 2016; Mei et al., 2018). The breadth-to-depth ratio *B/H* of the middle segment decreased from 1.20×10^3 to 1.06×10^3. That of the lower segment decreased from 5.67×10^3 to 3.69×10^3 (Table 4). The channel was narrowed and deepened.

During the ebb tide, flow was concentrated within the deep channel. The numerical simulation results (Lyu et al., 2019) showed that, after reclamations, the ratio of the water transport through NC to that through SB has increased from 45% to 50%. Taking the spring tide in the dry season as an example, the values of the dominant flow coefficient at station BG1 in 2003 was approximately 0.5 (Figure 5a), so the stagnation point was located close to this station. However, flow at both BG1 and BG 2 was obviously ebb dominant in 2018 (Figures 5c and 5d), thereby revealing a downstream shift of the stagnation point. The numerical simulation results (Lyu et al., 2019) showed that, after the constructions of reclamations, the salinity within channel on the south of the NC decreases in the dry season. Furthermore, the saline wedges moved seaward and the 5 PSU salinity isocline moved to the middle of HESP at slack tide. Due to the estuarine circulation resulting from the longitudinal density gradient, a large amount of sediment was deposited in the TMZ, which occurred at the end of the salt tongue (Shen et al., 1992). These findings explain the seaward shift of the landward boundary of the TMZ (Figure 8).

5.3. Decline of tidally averaged SSC near the landward boundary of the TMZ

In the datasets of 2003 and 2018, variations of tidal ranges varied from 0.55 to 0.69 m (Table 3). They were less than variations of tidal ranges between spring and neap tide in the same year (1.07 m and 1.78 m, respectively). The effect of the tidal range on the vertical distribution of SSC could not be considered. Following an earlier study by Liu et al. (2014), the shape of the vertical profile of tidally averaged SSC was only related to the dynamics of runoff, tide and the characteristics of surface sediments. The ratio of tidally averaged SSC in the surface and bottom layers were calculated to describe the shape of vertical profile.

During spring tide, the ratio of tidally averaged SSC in the surface and bottom layers in BG2 decreased from 3.38 in 2003 to 1.74 in 2018 (Figures 7b and 7e). During neap tide, the ratio of tidally averaged SSC in the surface and bottom layers in BG2 decreased from 6.11 in 2003 to 1.66 in 2018 (Figures 7b and 7e). The tidally averaged SSC near the bottom decreased, which resulted in the decrease of the tidally averaged SSC in the middle segment.

This can be understood as follows. Owing to the enhancement of the ebb tide resulting from both the narrowing and fixing of channels associated with the reclamation projects and the interception of sediment flow from the shoal caused by the HESP, the source of fine-grained sediment in the deep channel has been reduced (Liu et al., 2014; Li et al., 2019). This resulted in the observed coarsening of surface sediments in the deep channel of the middle segment in the dry season, where also the landward boundary of the TMZ was located. From 2003 to 2015, in the flood season, the median particle size of surface sediments in the middle segment of NC increased from 127.4 μm to 193.94 μm (Liu et al., 2010; Li, et al., 2019). This trend was similar to that during the dry season. The consequence was a weakening of the sediment resuspension. The tidally averaged

SSC on the bottom at station BG2 in 2018 was significantly lower than that in 2003 and this led to a decline of the depth-mean of tidally averaged SSC at station BG2 (Figures 7b and 7e). The landward boundary of the TMZ, which was in the 2 km seaward of station BG2, has moved 6 km seaward from the area. However, due to the replenishment of fine-grained sediment from the tidal flat and sea, the grain size of surface sediments in lower segment is now finer (Zhu et al., 2016; Mei et al., 2018). The depth-mean of tidally averaged SSC of station BG4 (Figure 7f), which was located near the core of the TMZ, has not significantly changed compared with that of BG3, which was also near the core of the TMZ (Figure 7c).

A conceptual model of spatial changes in the TMZ in response to reclamation was proposed based on the above analysis (Figure 8). In the middle segment, the deepened and narrowed channel caused by reclamations intensified the ebb-dominance and induced seaward migration of the stagnation point. In addition, surface sediment in the deep channel coarsened in response to the enhancement of ebb flow. The tidally averaged SSC near the bottom and the depth-mean of tidally averaged SSC declined due to the decrease in resuspension. This all led to the seaward movement of the landward boundary of the TMZ. However, there were little variation in flow dominance and characteristics of bed sediment in outer estuary, which resulted from strong tide flow and replenishment of fine-grained sediment from the tidal flat and sea. Therefore, seaward boundary of TMZ was less affected by reclamations.

As an improvement with respect to previous studies (Jiang et al., 2013), impacts of runoff, tidal condition on spatial distribution of SSSC were considered in the collection of remote sensing images. Due to the retaining effect of large-scale projects in the basin, there has been a continuous reduction of the SSSC in Yangtze Estuary (YE). The SSSC was converted into RSSSC to avoid the influence of the overall reduction in SSSC on determining the TMZ. However, the number of images obtained with the same river discharge and tidal condition was limited, within the remote sensing images obtained by Landsat in the last two decades. Six images were retrieved at times that there were similar river discharges and tidal conditions and few clouds.

As a next step, it would be interesting to further quantify the influence of bathymetric configuration on estuarine circulation and sediment transport with a numerical model, but this is beyond the scope of the present study.

6. Conclusions

The key message of this study is that reclamation projects conducted in estuaries can cause dramatic changes in the geometry of channels and can thus affect the river and tidal flow and thereby cause spatial changes in the TMZ. This study focused on the NC of the YE, which has been strongly affected by reclamation in the past two decades. The main conclusions are listed below.

1) The narrowed and fixed channel caused by reclamation has induced erosion of the deeper channel and deposition on the tidal flat from 2007 to 2018. Erosion has been intensified below a depth of -5 m in middle and lower segments and lower segment has been transformed from one of net deposition to an area of net erosion. Deposition has occurred on the shoal near the north bank in the middle and lower segments. The average channel width has decreased by 0.86-2.74 km, while the average depth has increased by 0.19-3.72 m.

2) After construction of the large-scale reclamation projects, *ASSSC* within the TMZ in NC decreased during both the spring tide and neap tide in the dry season. From 2006 to 2019, the landward boundary of the TMZ moved seaward by 6 km and the location of the seaward boundary

presently wanders within a 3 km range from 122° 12' E to 122° 14' E during spring tide. The landward boundary of the TMZ has moved seaward by 17 km and the seaward boundary of the TMZ wanders in the range of 122° 23' to 122° 24' during the neap tide. The *SSSC* within the TMZ during neap tide is lower than that in spring tide, and the TMZ during neap tide is located downstream of that during spring tide.

3) Ebb dominance has been enhanced due to deepening and narrowing of the channel that resulted from reclamations and this has induced the seaward movement of the stagnation point that is located close to the core of the TMZ. In addition, bed sediment has coarsened and its resuspension is thus weakened. Consequently, the bottom tidally averaged SSC in middle segment has decreased by 0.59 kg m^{-3} over spring tide and 0.77 kg m^{-3} over neap tide, which has resulted in a decline in the depth-mean of the tidally averaged SSC. All of these factors have caused the landward boundary of the TMZ to move seawards.

Acknowledgements

Thanks to Dr. Li Weihua and Dr. Zhang Erfeng, who led the in-situ observations. This work was supported by the National Natural Science Foundation of China-The Netherlands Organization for Scientific Research-Engineering and Physical Sciences Research Council (NSFC-NWO-EPSRC) (51761135023, EP/R02491X/1) and the China Geological Survey (DD20190260).

References

Burchard, H., Schuttelaars, H. M., Ralston, D.K., 2018. Sediment Trapping in Estuaries. Annu. Rev.

Mar. Sci., 10, 371-395. https://doi.org/10.1146/annurev-marine -010816-060535.

Cheng, H.Q., Chen, J.Y., Chen, Z.J., Ruan, R.L., Xu, G.Q., Zeng, G., Zhu, J.R., Dai, Z.J., Chen, X.Y., Gu, S.H., Zhang, X.L., Wang, H.M., 2018. Mapping Sea Level Rise Behavior in an Estuarine Delta System: A Case Study along the Shanghai Coast. Engin. 4, 156-163. https://doi.org/10.1016/J.eng.2018.02.002.

Cheng, Z.X., Jalon, R.I., Wang, X.H., Liu, Y., 2020. Impacts of land reclamation on sediment transport and sedimentary environment in a macro-tidal estuary. Estuar. Coast. Shelf Sci. 242. https://doi.org/10.1016/j.ecss.2020.106861.

de Jonge, V.N., Schutterlaars, H.M., van Beusekom, J.E.E., Talke, S.A., de Swart, H.E., 2014. The influence of channel deepening on estuarine turbidity levels and dynamics, as exemplified by the Ems estuary. Estuar. Coast. Shelf Sci. 139, 46-59. https://doi.org/10.1016/j.ecss.2013.12.030.

Doxaran, D., Froidefond, J.M., Castaing, P., Babin, M., 2009. Dynamics of the turbidity maximum zone in a macrotidal estuary (the Gironde, France): Observations from field and MODIS satellite data. Estuar. Coast. Shelf Sci. 81, 321-332. https://doi.org/10.1016/j.ecss.2008.11.013.

Du, J.L., Yang, S.L., Feng, H., 2016. Recent human impacts on the morphological evolution of the Yangtze River delta foreland: A review and new perspectives. Estuar. Coast. Shelf Sci. 181, 160-169. https://doi.org/10.1016/j.ecss.2016.08.025.

Folk, R.L., Andrews, P.B., Lewis, D.W., 1970. Detrital sedimentary rock classification and nomenclature for use in New Zealand. New. Zeal. Geol. Geop. 13(4), 937-968, https://doi.org/10.1080/00288306.1970.10418211.

Gao, G.D., Wang, X.H., Bao, X.W., Song, D.H., Lin, X.P., Qiao, L.L., 2018. The impacts of land reclamation on suspended-sediment dynamics in Jiaozhou Bay, Qingdao, China. Estuar. Coast.

Shelf Sci. 206, 61-75. https://doi.org/10.1016/j.ecss.2017.01.012.

Gebhardt, A.C., Schoster, F., Gaye, H., Beeskow, B., Rachold, V., Unger, D., Ittekkot, V., 2005. The turbidity maximum zone of the Yenisei River (Siberia) and its impact on organic and inorganic proxies. Estuar. Coast. Shelf Sci. 65, 61-73. https://doi.org/10.1016/j.ecss.2005.05.007.

Guo，L.C., Su, N., Zhu, C.Y., He, Q., 2018. How have the river discharges and sediment loads changed in the Changjiang River basin downstream of the Three Gorges Dam? J. Hydrol. 560, 259-274. https://doi.org/10.1016/j.jhydrol.2018.03.035.

Jiang, C.J., de Swart, H.E., Li, J.F., Liu, G.F., 2013. Mechanisms of along-channel sediment transport in the North Passage of the Yangtze Estuary and their response to large-scale interventions. Ocean Dynam. 63, 283-305. https://doi.org/10.1007/s10236-013-0594-4.

Jiang, X.Z., Lu, B., He, Y.H., 2013. Response of the turbidity maximum zone to fluctuations in sediment discharge from river to estuary in the Changjiang Estuary (China). Estuar. Coast. Shelf Sci. 131, 24-30. https://doi.org/10.1016/j.ecss.2013.07.003.

Lange. X., Burchard, H., 2019. The relative importance of wind straining and gravitational forcing in driving exchange flows in tidally energetic estuaries. J. Phys. Oceanogr. 49(3), 723-736. https://doi.org/10.1175/JPO-D-18-0014.1

Li, J.F., Zhang, C., 1998. Sediment resuspension and implications for turbidity maximum in the Changjiang Estuary. Mar. Geol. 148, 117-124. https://doi.org/10.1016/S0025-3227(98)00003-6.

Li, Z.H., Jia, J.J., Wu, Y.S., Zong, H.B., Zhang, G.A., Wang, Y.P., Yang, Y., Zhou, L., Gao. S., 2019. Vertical distributions of suspended sediment concentrations in the turbidity maximum zone of the periodically and partially stratified Changjiang Estuary. Estuar. Coast. 42, 1475-1490. https://doi.org/10.1007/s12237-019-00605-2.

Liu, H., He. Q., Wang, Z.B., Weltje, J.G., Zhang, J., 2010. Dynamics and spatial variability of near-bottom sediment exchange in the Yangtze Estuary, China. Estuar. Coast. Shelf Sci. 86, 322-330. https://doi.org/10.1016/j.ecss.2009.04.020.

Liu, J.H., Yang, S.L., Zhu, Q., Zhang, J., 2014. Controls on suspended sediment concentration profiles in the shallow and turbid Yangtze Estuary. Cont. Shelf Res. 90, 96-108. https://doi.org/10.1016/j.csr.2014.01.021.

Luan, H.L., Ding, P.X., Wang, Z.B., Ge, J.Z., Yang, S.L., 2016. Decadal morphological evolution of the Yangtze Estuary in response to river input changes and estuarine engineering projects. Geomorphology 265, 12-23. https://doi.org/10.1016/j.geomorph.2016.04.022.

Lyu, H.H., Zhu, J.R., 2019. Impacts of tidal flat reclamation on saltwater intrusion and freshwater resources in the Changjiang Estuary. J. Coastal. Res. 35(2), 314-321. https://doi.org/10.2112/JCOASTRES-D-18-00077.1.

Mei, X.F., Dai, Z.J., Wei, W., Li, W.H., Wang, J., Sheng, H., 2018. Secular bathymetric variations of the North Channel in the Changjiang (Yangtze) Estuary, China, 1880-2013: Causes and effects. Geomorphology 303, 30-40. https://doi.org/10.1016/j.geomorph.2017.11.014.

Mitchell, S.B., 2013. Turbidity maxima in four macrotidal estuaries. Ocean Coast. Manage. 79, 62-69. https://doi.org/10.1016/j.ocecoaman.2012.05.030.

Pye K., Blott, S.J., 2014. The geomorphology of UK estuaries: The role of geological controls, antecedent conditions and human activities. Estuar. Coast. Shelf Sci. 150, 196-214. https://doi.org/10.1016/j.ecss.2014.05.014

Shen, F., Zhou, Y.X., Li, J.F., He, Q., Verhoef, W., 2013. Remotely sensed variability of the suspended sediment concentration and its response to decreased river discharge in the Yangtze estuary and adjacent coast. Cont. Shelf Res. 69, 52-61. https://doi.org/10.1016/j.csr.2013.09.002.

Shen, H.T., Zhang, C.L., 1992. Mixing of salt water and fresh water in the Changjiang River estuary and its effects on suspended sediment. Chinese Geogr. Sci. 2, 373–381. https://doi.org/10.1007/BF02664568.

van der Wal, D., Pye, K., Neal, A., 2002. Long-term morphological change in the Ribble Estuary, northwest England. Mar. Geol. 189(3-4), 249-266. https://doi.org/10.1016/S0025-3227(02)00476-0.

van Maren, D.S., Oost, A.P., Wang, Z.B., Vos, P.C., 2016. The effect of land reclamations and sediment extraction on the suspended sediment concentration in the Ems Estuary. Mar. Geol. 376, 147-157. https://doi.org/10.1016/j.margeo.2016.03.007.

Wackerman, C., Hayden, A., Jonik, J., 2017. Deriving spatial and temporal context for point measurements of suspended-sediment concentration using remote-sensing imagery in the Mekong Delta. Cont. Shelf Res. 147, 231-245. https://doi.org/10.1016/j.csr.2017.08.007.

Wang, Y.H., Dong, P., Oguchi, T., Chen, S.L., Shen, H.T., 2013. Long-term (1842–2006) morphological change and equilibrium state of the Changjiang (Yangtze) Estuary, China. Cont. Shelf Res. 56, 71-81. https://doi.org/10.1016/j.csr.2013.02.006.

Webster, R., Oliver, M.A., 2007. Geostatistics for Environmental Scientists: Second Edition. John Wiley & Sons, Ltd, Chichester, pp.153-193.

Wei, W., Dai, Z.J., Mei, X.F., Liu, J.P., Gao, S., Li, S.S., 2017. Shoal morphodynamics of the Changjiang (Yangtze) estuary: Influences from river damming, estuarine hydraulic engineering and reclamation project. Mar. Geol. 386, 32-43. https://doi.org/10.1016/j.margeo.2017.02.013.

Williams, J., Lee, G.H., Shin, H.J., Dellapenna, T., 2015. Mechanism for sediment convergence in the anthropogenically altered microtidal Nakdong Estuary, South Korea. Mar. Geol. 369, 79-90. https://doi.org/10.1016/j.margeo.2015.08.004.

Wu, J.X., Liu, J.T., Wang, X., 2012. Sediment trapping of turbidity maxima in the Changjiang Estuary. Mar. Geol. 303-306, 14-25. https://doi.org/10.1016/j.margeo.2012.02.011.

Wu, S.H., Cheng, H.Q., Xu, Y.J., Li, J.F., Zheng, S.W., 2016. Decadal changes in bathymetry of the Yangtze River Estuary: Human impacts and potential saltwater intrusion. Estuar. Coast. Shelf Sci. 182, 158-169. https://doi.org/10.1016/j.ecss.2016.10.002.

Yang, S.L., Liu, Z., Dai, S.B., Gao, Z.X., Zhang, J., Wang, H.J., Luo, X.X., Wu, C.S., Zhang, Z., 2010. Temporal variations in water resources in the Yangtze River (Changjiang) over the Industrial Period, based on reconstruction of missing monthly discharges. Water Resour. Res. 46, W10516. https://doi.org/10.1029/2009WR008589.

Zhang, E.F., Gao, S., Savenjie, H.H.G., Si, C.Y., Cao, S., 2019. Saline water intrusion in relation to strong winds during winter cold outbreaks: North Branch of the Yangtze Estuary. J. Hydrol. 574, 1099-1109. https://doi.org/10.1016/j.jhydrol.2019.04.096

Zhang, Y.Z., Chen, R.S., Wang, Y., 2020. Tendency of land reclamation in coastal areas of Shanghai from 1998 to 2015. Land Use Pol. 91. https://doi.org/10.1016/j.landusepol.2019.104370.

Zhao, J., Guo, L.C., He, Q., Wang, Z.B., van Maren, D.S., Wang, X.Y., 2018. An analysis on half century morphological changes in the Changjiang Estuary: Spatial variability under natural processes and human intervention. J. Marine Syst., 181, 25-36. https://doi.org/10.1016/j.jmarsys.2018.01.007.

Zheng, S.W., Cheng H.Q., Shi, S.Y., Xu, W., Zhou, Q.P., Jiang, Y.H., Zhou, F.N., Cao, M.X., 2018. Impact of anthropogenic drivers on subaqueous topographical change in the Datong to

Xuliujing reach of the Yangtze River. Sci. China Earth Sci. 61, 940-950. https://doi.org/10.1007/s11430-017-9169-4.

Zhu, L., He, Q., Shen, J., Wang, Y., 2016. The influence of human activities on morphodynamics and alteration of sediment source and sink in the Changjiang Estuary. Geomorphology 273, 52-62. https://doi.org/10.1016/j.geomorph.2016.07.025.

Figure captions

Figure 1. Map showing the study area, with in (a) the location of Yangtze Estuary in China and the locations of Datong and Sheshan gauging stations; (b) Yangtze Estuary; (c) North Channel.

Figure 2. Changes in erosion-deposition patterns of North Channel, negative refers to erosion and positive to deposition (a-c). The channel volumes below 0 m (d), -5 m (e) and -10 m (f) isobaths. Changes in channel volume from 1995 to 2007 (g) and from 2007 to 2018 (h), the orange curve shows the changes of channel volume from 1995 to 2018.

Figure 3. The spatial distribution of surface suspended sediment concentration (SSSC) in the North Channel on 2006-11-06(a), 2010-01-17 (b) and 2019-12-12 (c). Panels (d-f): as panels (a-c), but for the spatial distribution of the relative surface suspended sediment concentration (RSSSC). The RSSSC was the ratio of SSSC to region-averaged SSSC within the North Channel. Panels (g-i): the distribution of RSSSC along the longitudinal profile (the red line in Figure 1c). The gray block is the range of turbidity maximum zone (the RSSSC > 1).

Figure 4. The spatial distribution of surface suspended sediment concentration surface (SSSC) in the North Channel on 2006-01-22 (a), 2013-11-25 (b) and 2017-12-22 (c). Panels (d-f): as panels (a-c), but for the spatial distribution of the relative surface suspended sediment concentration (RSSSC). The RSSSC was the ratio of SSSC to region-averaged SSSC within the North Channel. Panels (g-i): the distribution of RSSSC along the longitudinal profile (the red line in Figure 1c). The

gray block is the range of turbidity maximum zone (the RSSSC > 1).

Figure 5. Vertical profiles of the dominant flow coefficients *R* at stations BG1 (a) and BG2 (b) on 2003-02-18 (spring tide), 2003-02-24 (neap tide), at stations BG1 (c), BG2 (d) and BG4 (e) on 2018-04-18 (spring tide) and 2018- 04-22 (neap tide). If $R>0.5$ the flow is ebb-dominant, whereas if $R<0.5$ the flow is flood-dominant. Here, σ is relative depth ($\sigma = 0$ is the surface and $\sigma = -1$ the bottom).

Figure 6. Temporal variations of SSC (kg m^{-3}) at stations BG1 (a), BG2 (b), BG3 (c) on 2003-02-18 (spring tide), BG1 (d), BG2 (e), BG4 (f) on 2018-04-18 (spring tide), BG1 (g), BG2 (h), BG3 (i) on 2003-02-24 (neap tide), and BG1 (j), BG2 (k), BG4 (l) on 2018-04-22 (neap tide).

Figure 7. Vertical profiles of tidally averaged suspended sediment concentrations at stations BG1 (a), BG2 (b), BG3 (c) on 2003-02-18 (spring tide), 2003-02-24 (neap tide), at stations BG1 (d), BG2 (e), BG4 (f) on 2018-04-18 (spring tide) and 2018-04-22 (neap tide) (d-f). Here, σ is relative depth ($\sigma = 0$ is the surface and $\sigma = -1$ the bottom).

Figure 8. A conceptual model of the shift of the turbidity maximum zone in response to reclamations. In the cross section of the channel, the solid line and dashed line are the channel bed before and after reclamations respectively. The channel narrowed (blue horizontal arrow) and deepened (blue vertical arrow) resulted from the construction of reclamation (yellow cube). As a result, coefficient of flow dominance increased (purple curve in the first subpanel on the bottom left); the estuarine circulation (purple arrow) area moved seaward. The sediment resuspension (orange arrow)

decreased due to coarsening of surface sediment, the tidal average suspended sediment concentration (orange curve) on the bottom layer decreased (orange curve in the second subpanel on the bottom left) and the landward boundary of the turbidity maximum zone (the dash border) moved seaward.

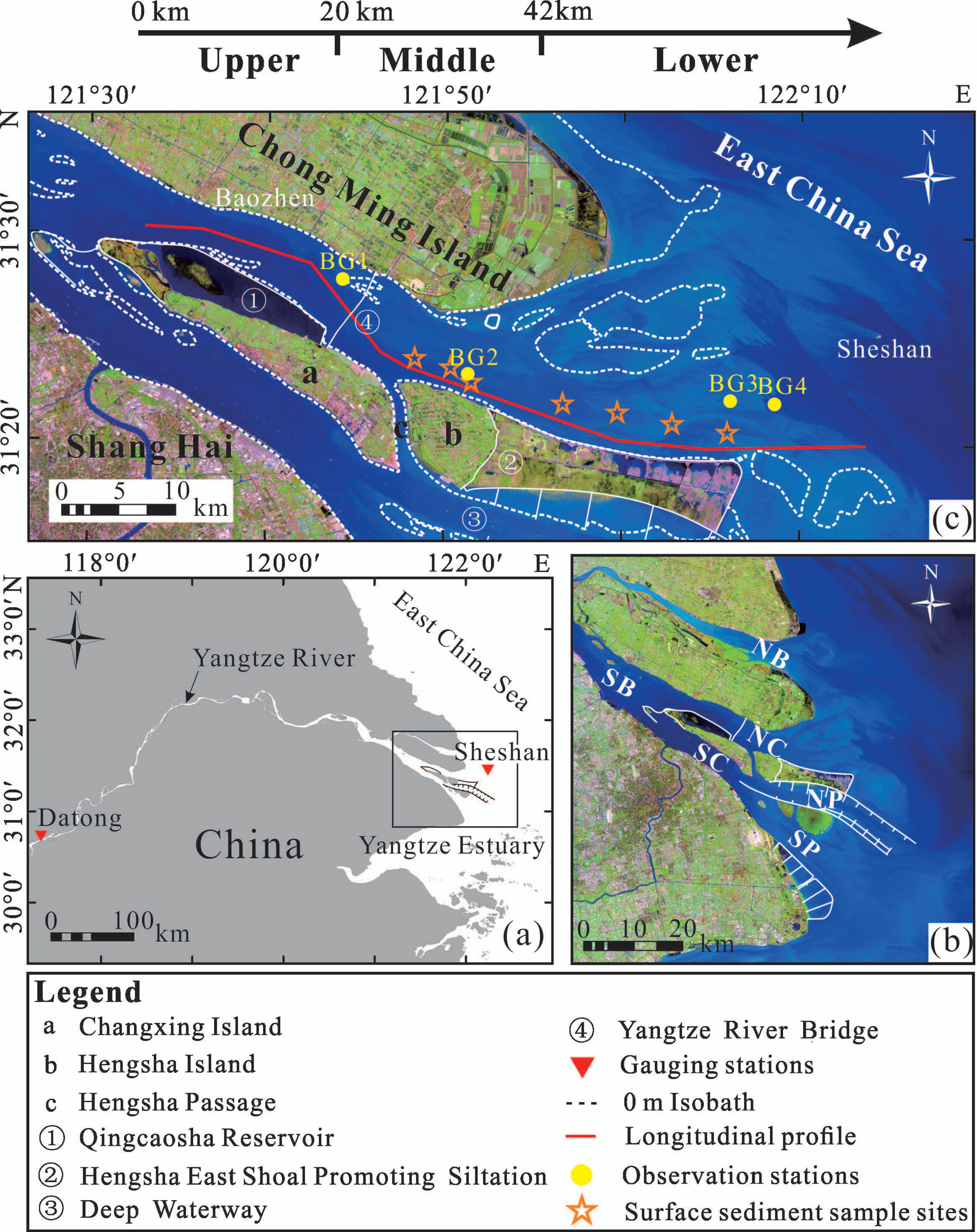

0 km
20 km
42km
Upper
Middle
Lower
121°30′
121°50′
122°10′
E
N
31°30′
31°20′
Chong Ming Island
East China Sea
Baozhen
BG1
BG2
BG3
BG4
Sheshan
Shang Hai
a
b
c
①
②
③
④
0 5 10 km
(c)
118°0′
120°0′
122°0′
33°0′N
32°0′
31°0′
30°0′
Yangtze River
East China Sea
Sheshan
Datong
China
Yangtze Estuary
0 100 km
(a)
NB
SB
NC
SC
NP
SP
0 10 20 km
(b)
Legend
a Changxing Island
b Hengsha Island
c Hengsha Passage
① Qingcaosha Reservoir
② Hengsha East Shoal Promoting Siltation
③ Deep Waterway
④ Yangtze River Bridge
Gauging stations
0 m Isobath
Longitudinal profile
Observation stations
Surface sediment sample sites

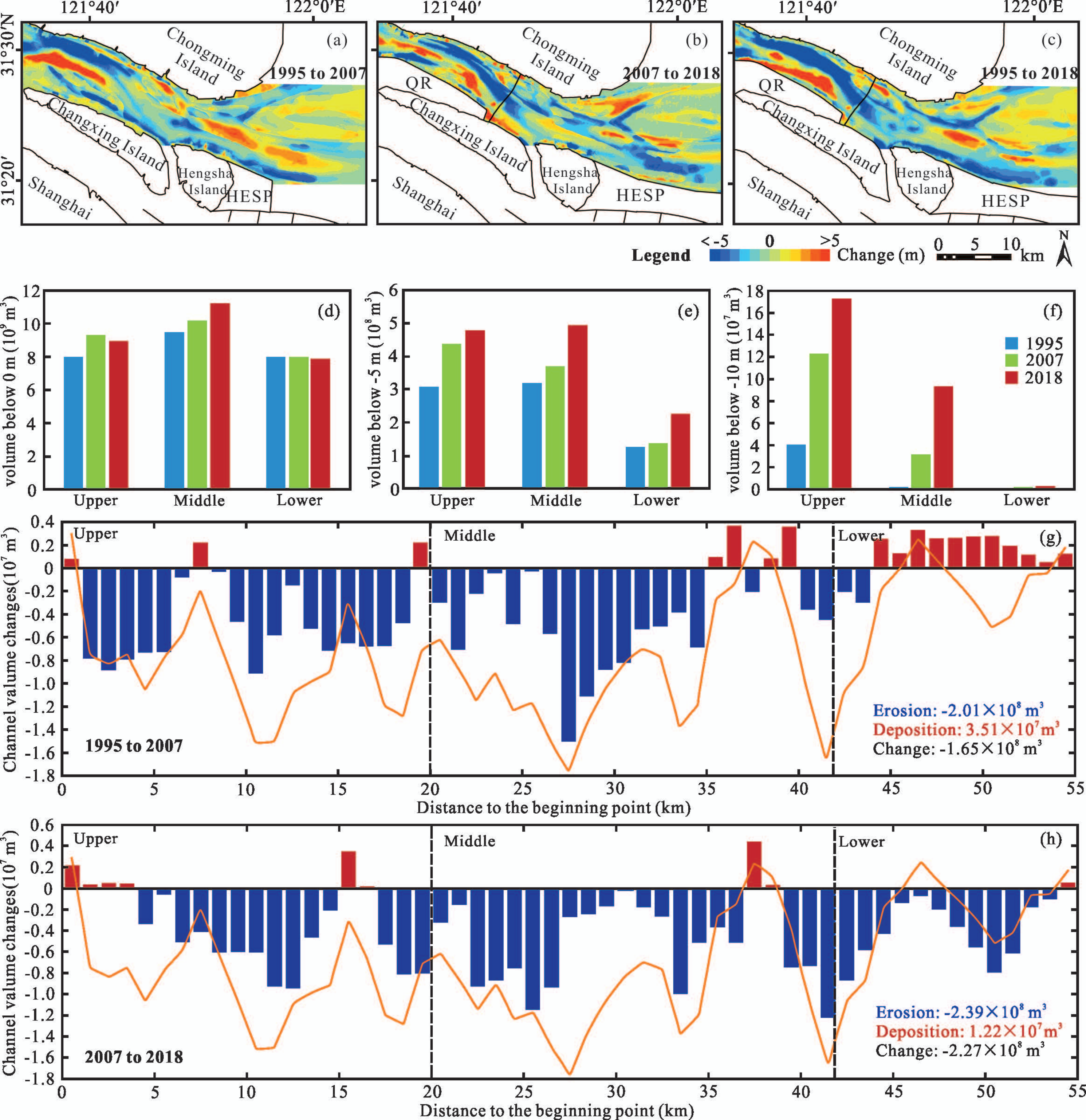

121°40′
122°0′E
31°30′N
31°20′
Chongming Island
Changxing Island
Hengsha Island
Shanghai
HESP
QR
(a) 1995 to 2007
(b) 2007 to 2018
(c) 1995 to 2018
Legend
<-5 0 >5 Change (m)
0 5 10 km
N
(d) volume below 0 m (10^9 m^3)
(e) volume below -5 m (10^8 m^3)
(f) volume below -10 m (10^7 m^3)
1995
2007
2018
Upper
Middle
Lower
(g)
Channel valume changes(10^7 m^3)
1995 to 2007
Erosion: -2.01×10^8 m^3
Deposition: 3.51×10^7 m^3
Change: -1.65×10^8 m^3
Distance to the beginning point (km)
(h)
2007 to 2018
Erosion: -2.39×10^8 m^3
Deposition: 1.22×10^7 m^3
Change: -2.27×10^8 m^3

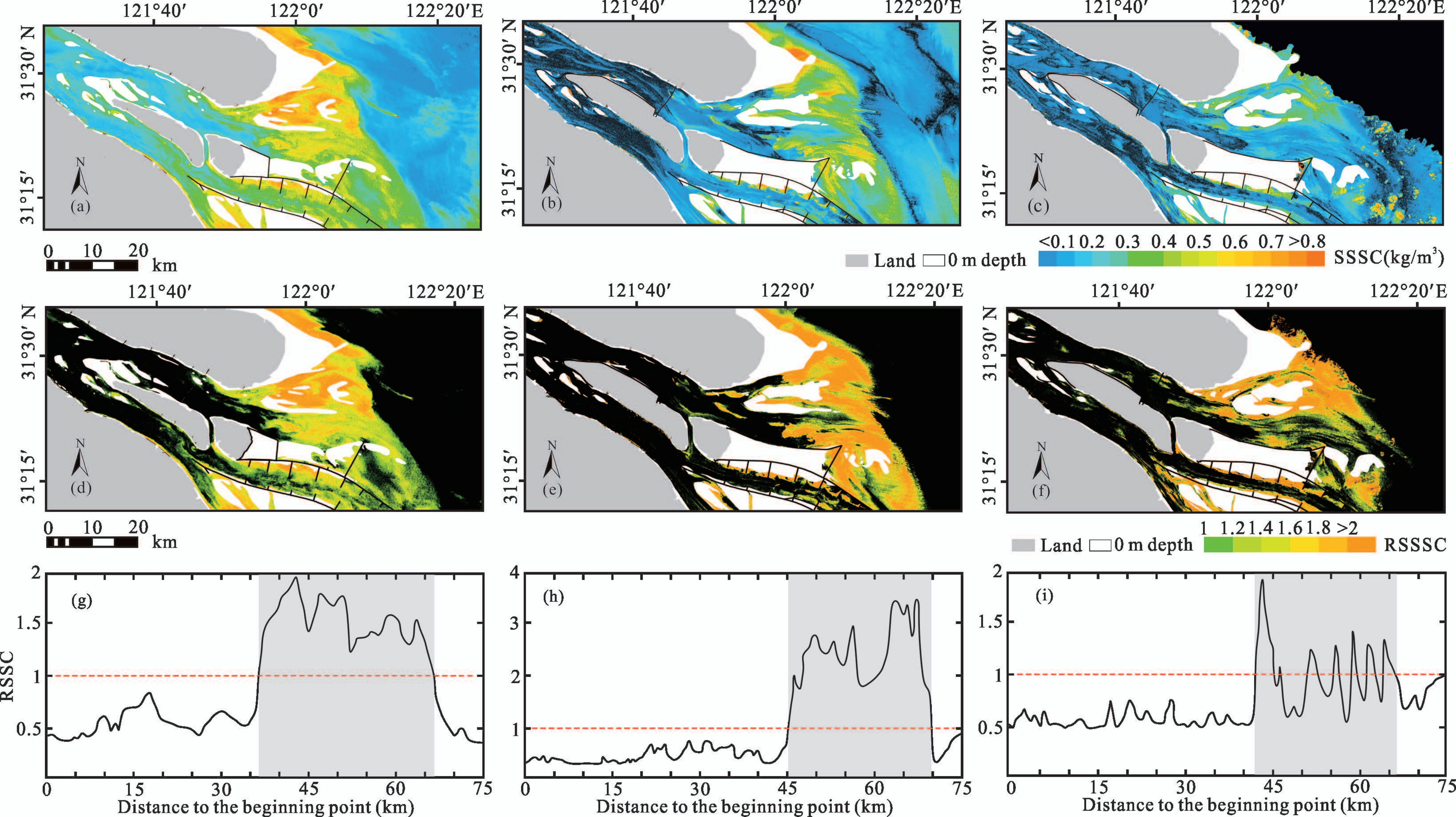

121°40′
122°0′
122°20′E
31°30′ N
31°15′
(a)
(b)
(c)
(d)
(e)
(f)
0 10 20 km
Land
0 m depth
<0.1 0.2 0.3 0.4 0.5 0.6 0.7 >0.8
SSSC(kg/m³)
1 1.2 1.4 1.6 1.8 >2
RSSSC
(g)
(h)
(i)
RSSC
Distance to the beginning point (km)

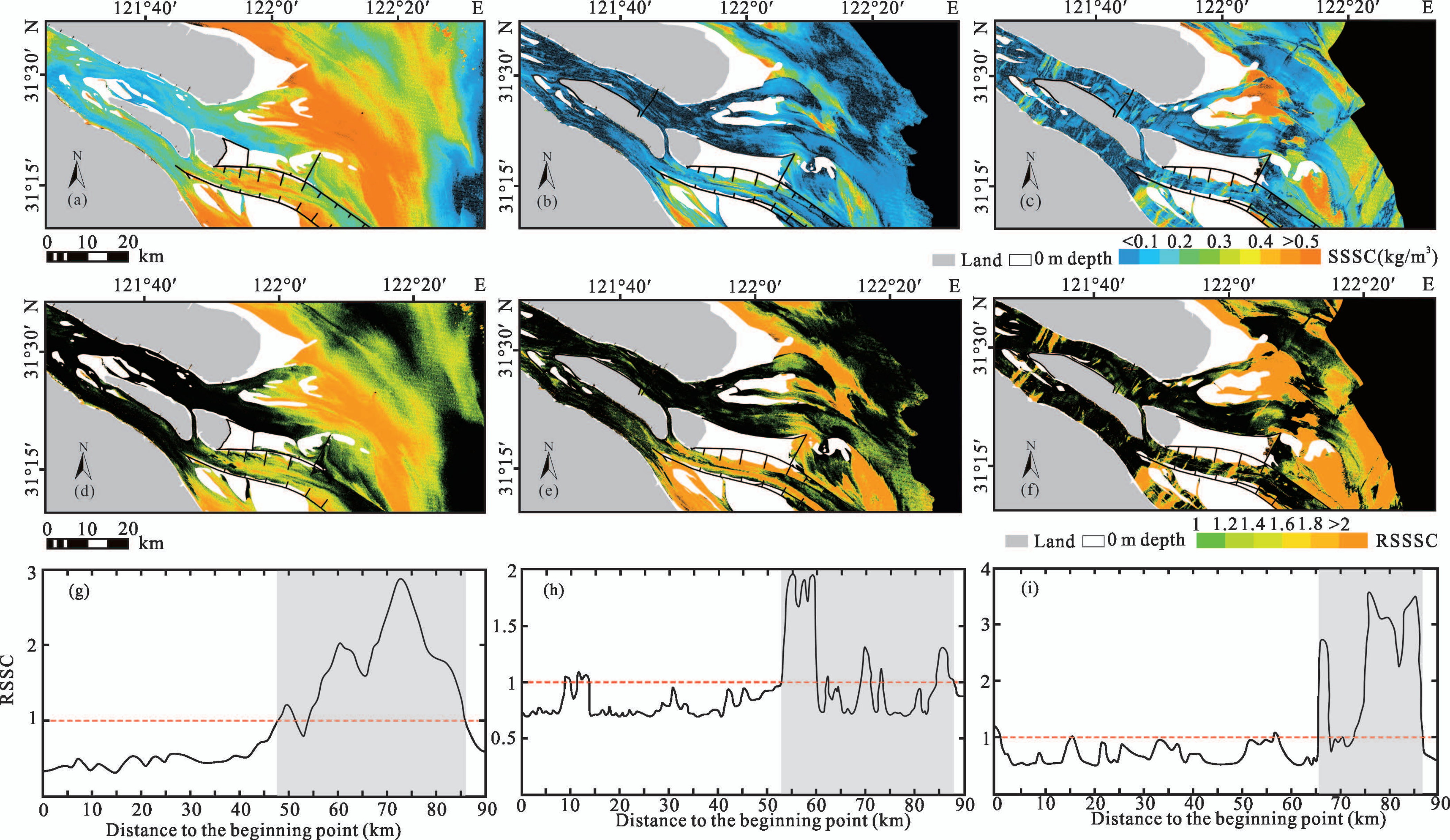
121°40′
122°0′
122°20′
E
N
31°30′
31°15′
(a)
(b)
(c)
(d)
(e)
(f)
0 10 20
km
Land
0 m depth
<0.1 0.2 0.3 0.4 >0.5
SSSC(kg/m³)
1 1.2 1.4 1.6 1.8 >2
RSSSC
(g)
(h)
(i)
RSSC
Distance to the beginning point (km)

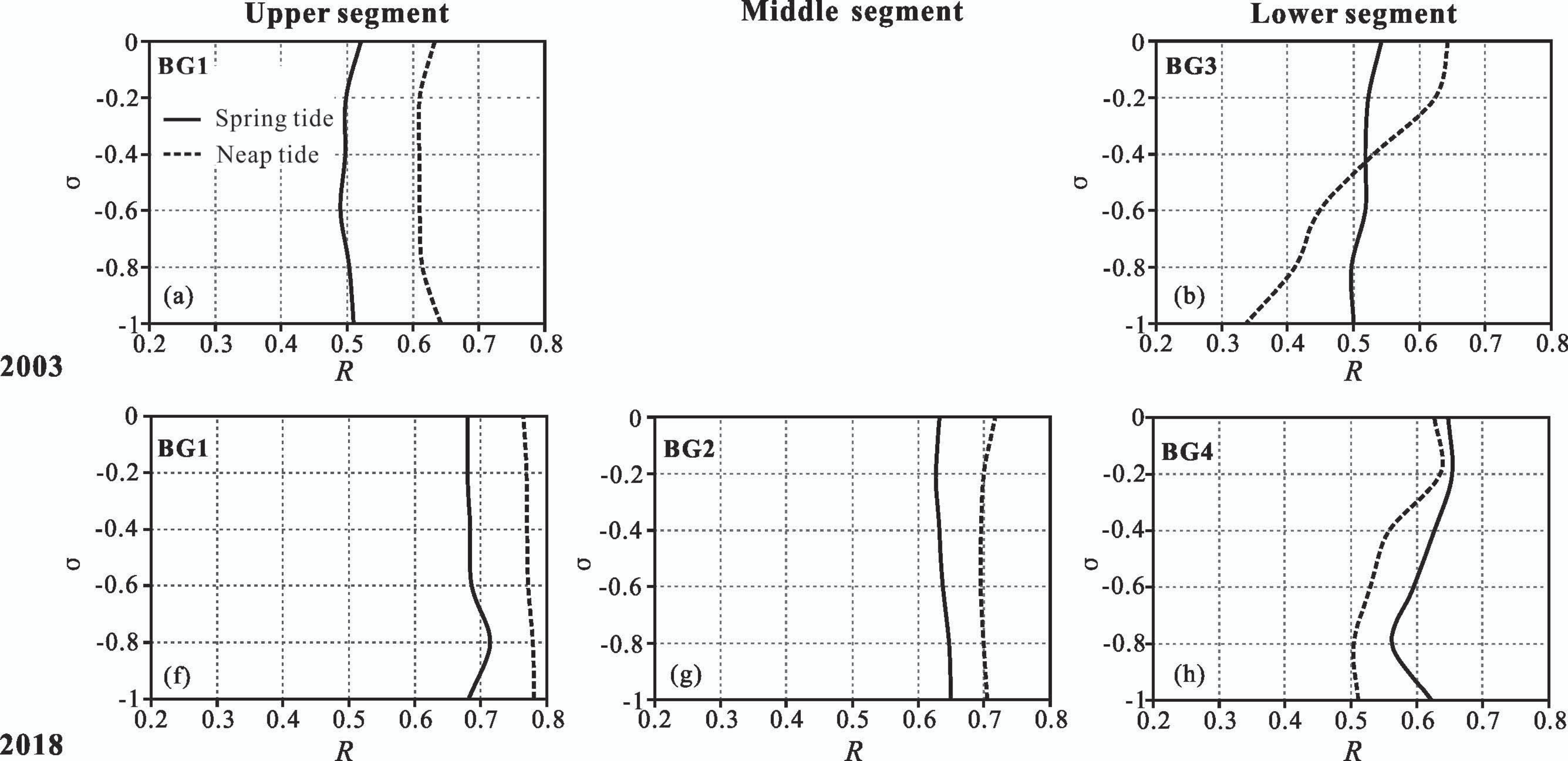
Upper segment
Middle segment
Lower segment
BG1
Spring tide
Neap tide
(a)
BG3
(b)
2003
BG1
(f)
BG2
(g)
BG4
(h)
2018
σ
R
0
-0.2
-0.4
-0.6
-0.8
-1
0.2
0.3
0.4
0.5
0.6
0.7
0.8

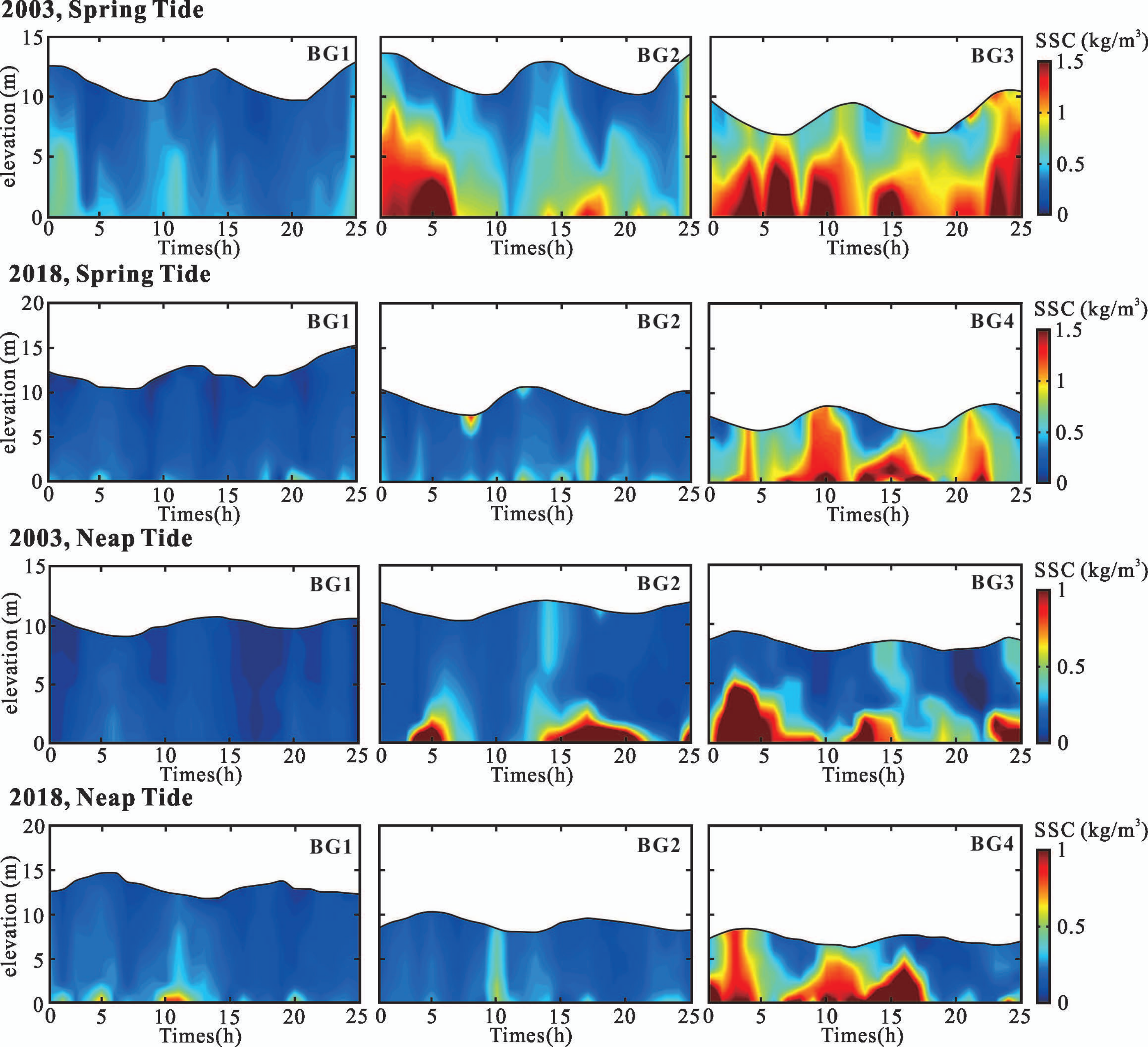
2003, Spring Tide
BG1
BG2
BG3
SSC (kg/m³)
2018, Spring Tide
BG1
BG2
BG4
SSC (kg/m³)
2003, Neap Tide
BG1
BG2
BG3
SSC (kg/m³)
2018, Neap Tide
BG1
BG2
BG4
SSC (kg/m³)
elevation (m)
Times(h)

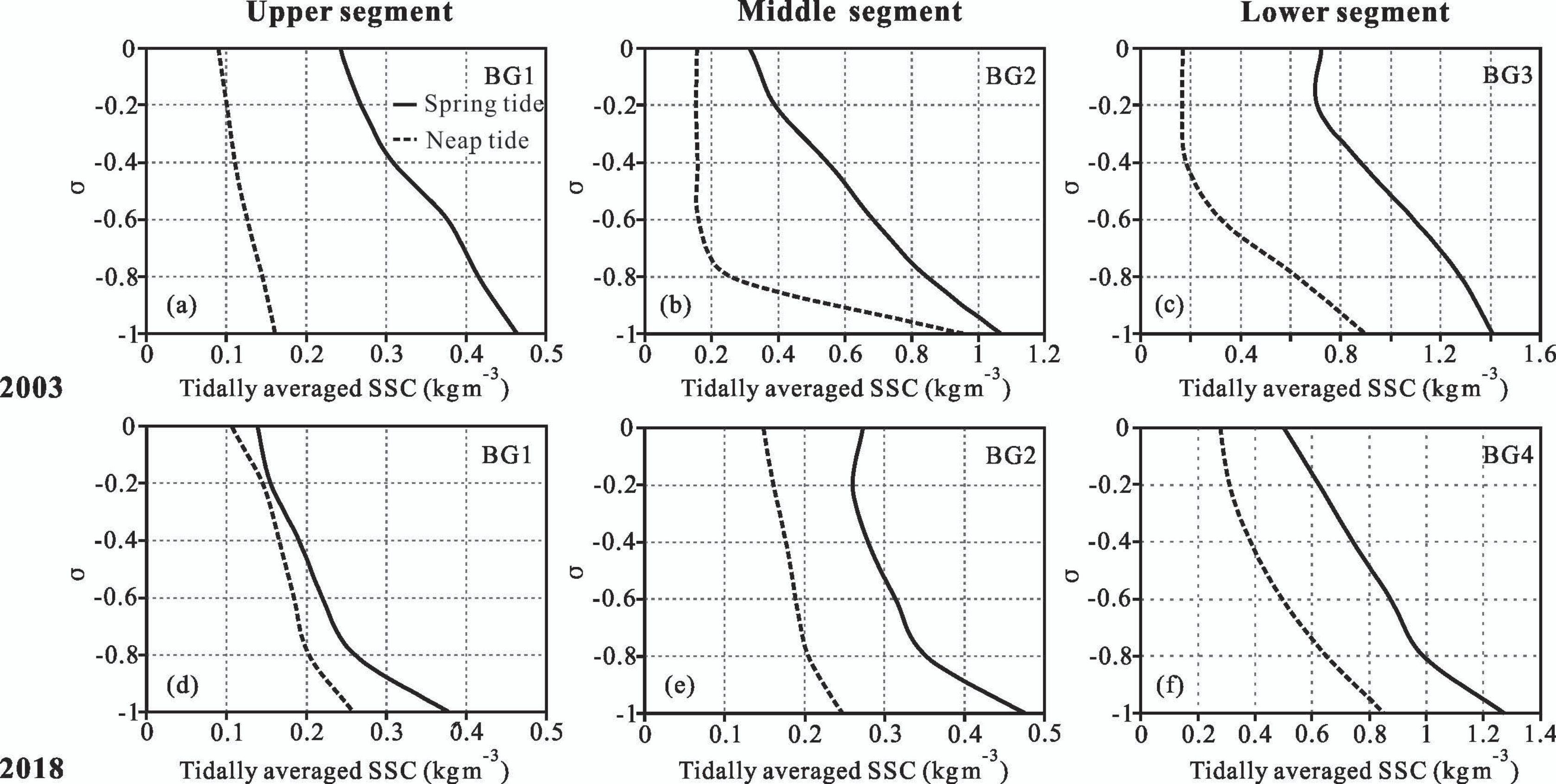

Upper segment
Middle segment
Lower segment
BG1
BG2
BG3
Spring tide
Neap tide
(a)
(b)
(c)
σ
2003
Tidally averaged SSC (kgm^-3)
BG1
BG2
BG4
(d)
(e)
(f)
2018

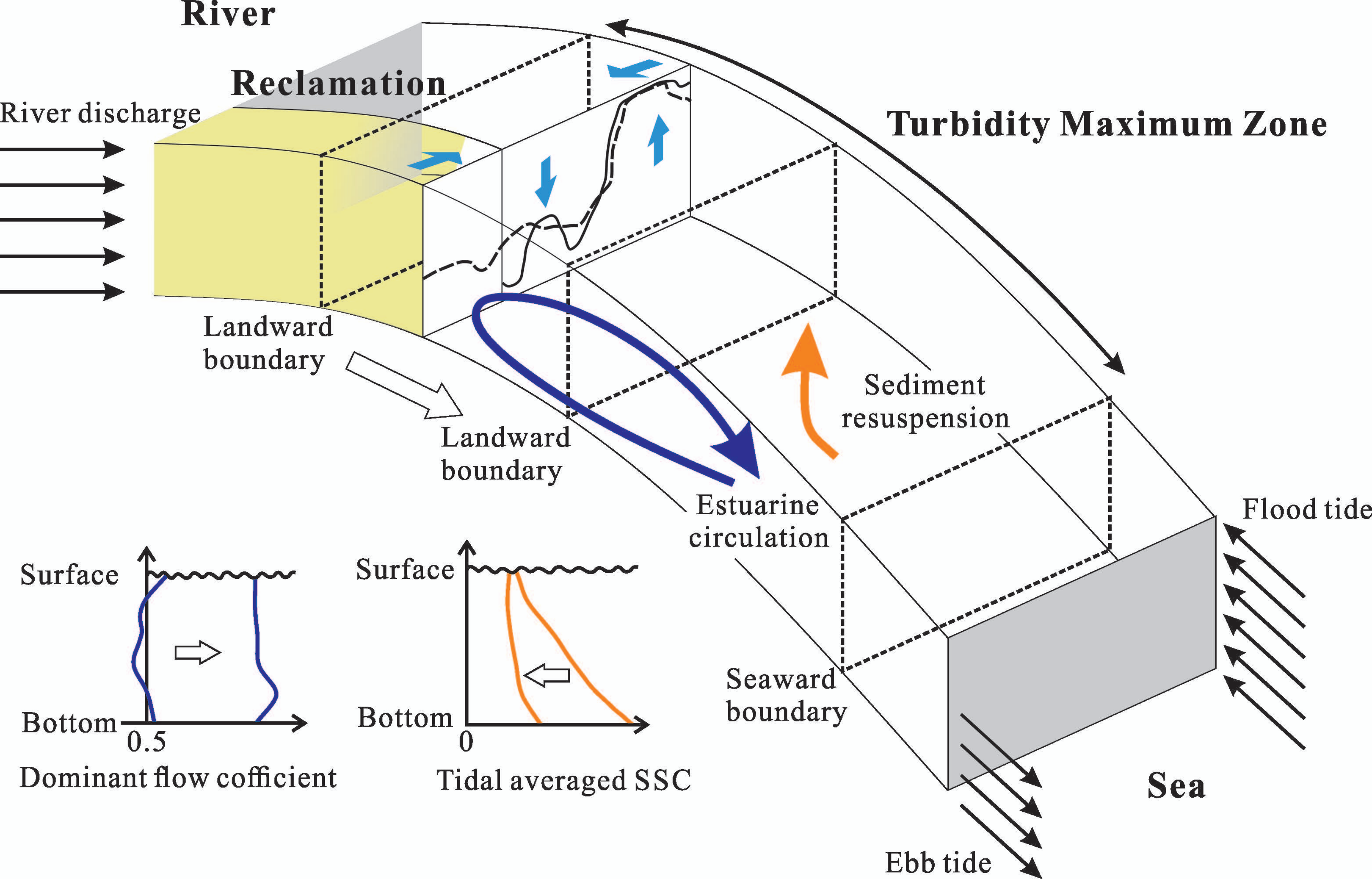
River
Reclamation
River discharge
Turbidity Maximum Zone
Landward boundary
Landward boundary
Sediment resuspension
Estuarine circulation
Flood tide
Seaward boundary
Sea
Ebb tide
Surface
Bottom
0.5
Dominant flow cofficient
Surface
Bottom
0
Tidal averaged SSC

Table 1. Engineering built in NC during past three decades.

Engineering	Location	Time
Diversion port	Upper segment of NC	2007-2009
Qingcaosha Reservoir	Upper segment of NC	2005-2009
Shanghai Yangtze Bridge	Upper segment of NC	2005-2007
Reclamation on the north bank of Changxing Island	North bank of Changxing Island	2007-2009
Chongming East Shoal Reclamation	Chongming East Shoal	1998-
Hengsha East Shoal Promoting Siltation project	Hengsha East Shoal	2007-

Table 2. Six Landsat images from 2006 to 2019.

Serial number	**Imaging data**	**Sensor**	**Mapping time (GMT)**	**Flow in Datong**	**Flood/Ebb**	**Tide type**
a	2006-01-22	Landsat 7 ETM	02:14:56.50	16800	Flood tide	Neap
b	2006-11-06	Landsat 7 ETM	02:14:49.55	16800	Ebb tide	Spring
c	2011-02-05	Landsat 7 ETM	02:18:24.90	15600	Flood tide	Spring
d	2013-12-11	Landsat 7 ETM	02:21:21.48	11200	Ebb tide	Neap
e	2018-02-08	Landsat 7 ETM	02:26:35.25	17700	Flood tide	Neap
f	2019-12-12	Landsat 7 ETM	02:06:56.02	11100	Ebb tide	Spring

Table 3. Date, location, tidal conditions, wave conditions, discharges in Datong and profiles.

Stations	Date	Distance from starting point（km）	Tidal condition	Discharge in Datong($m^3 \cdot s^{-1}$)	Channel segment	Daily averaged tidal range (m)	Daily averaged wave height (m)	Profiles
BG1	2003-02-18	20	Spring tide	16385	Upper	2.95	0.74-1.17	SSC profiles
	2003-02-24		Neap tide	21000		1.43	0.55-0.86	Velocity profiles
BG2	2003-02-18	34	Spring tide	16385	Middle	3.10	0.74-1.17	SSC profiles
	2003-02-24		Neap tide	21000		1.32	0.55-0.86	
BG3	2003-02-18	56	Spring tide	16385	Lower	3.05	0.74-1.17	SSC profiles
	2003-02-24		Neap tide	21000		1.29	0.55-0.86	Velocity profiles
BG1	2018-04-18	20	Spring tide	17300	Upper	3.64	0.73-0.98	SSC profiles
	2018-04-22		Neap tide	20400		2.22	0.53-0.93	Velocity profiles
BG2	2018-04-18	34	Spring tide	17300	Middle	2.94	0.73-0.98	SSC profiles
	2018-04-22		Neap tide	20400		1.87	0.53-0.93	Velocity profiles
BG4	2018-04-18	65	Spring tide	17300	Lower	2.92	0.73-0.98	SSC profiles
	2018-04-22		Neap tide	20400		1.62	0.53-0.93	Velocity profiles

Table 4. Average breadth and depth of NC in 1995, 2007and 2018.

	Average breadth *B*（km）			Average depth *H* (m)			*B/H* (×10^3)		
	1995	2007	2018	1995	2007	2018	1995	2007	2018
Upper segment	8.03	7.94	5.29	5.35	6.29	9.07	1.50	1.26	0.58
Middle segment	8.26	7.62	7.53	5.47	6.37	7.10	1.51	1.20	1.06
Lower segment	15.07	17.68	14.21	3.66	3.12	3.85	4.12	5.67	3.69